Accepted for publication in ApJ.
Preprint typeset using LaTeX style emulateapj v. 5/2/11

EXCITATION MECHANISMS FOR HCN (1–0) AND HCO^+ (1–0) IN GALAXIES FROM THE GREAT OBSERVATORIES ALL-SKY LIRG SURVEY[1]

G. C. Privon[2,3,4], R. Herrero-Illana[5], A. S. Evans[2,6], K. Iwasawa[7], M. A. Perez-Torres[5], L. Armus[8], T. Díaz-Santos[8,9], E. J. Murphy[10], S. Stierwalt[2], S. Aalto[11], J. M. Mazzarella[10], L. Barcos-Muñoz[2], H. J. Borish[2], H. Inami[13], D.-C. Kim[6], E. Treister[3], J. A. Surace[8], S. Lord[14], J. Conway[11], D. T. Frayer[12], and A. Alberdi[5]

Accepted for publication in ApJ.

ABSTRACT

We present new IRAM 30m spectroscopic observations of the $\sim$ 88 GHz band, including emission from the CCH (N = 1 $\rightarrow$ 0) multiplet, HCN (J = 1 $\rightarrow$ 0), HCO^+ (J = 1 $\rightarrow$ 0), and HNC (J = 1 $\rightarrow$ 0), for a sample of 58 local luminous and ultraluminous infrared galaxies from the Great Observatories All-sky LIRG Survey (GOALS). By combining our new IRAM data with literature data and Spitzer/IRS spectroscopy, we study the correspondence between these putative tracers of dense gas and the relative contribution of active galactic nuclei (AGN) and star formation to the mid-infrared luminosity of each system. We find the HCN (1–0) emission to be enhanced in AGN-dominated systems ($\langle\ L'_{HCN\ (1–0)}/L'_{HCO^+\ (1–0)}\ \rangle = 1.84$), compared to composite and starburst-dominated systems ($\langle\ L'_{HCN\ (1–0)}/L'_{HCO^+\ (1–0)}\ \rangle = 1.14$, and 0.88, respectively). However, some composite and starburst systems have $L'_{HCN\ (1–0)}/L'_{HCO^+\ (1–0)}$ ratios comparable to those of AGN, indicating that enhanced HCN emission is not uniquely associated with energetically dominant AGN. After removing AGN-dominated systems from the sample, we find a linear relationship (within the uncertainties) between $\log_{10}(L'_{HCN\ (1–0)})$ and $\log_{10}(L_{IR})$, consistent with most previous findings. $L'_{HCN\ (1–0)}/L_{IR}$, typically interpreted as the dense gas depletion time, appears to have no systematic trend with L_{IR} for our sample of luminous and ultraluminous infrared galaxies, and has significant scatter. The galaxy-integrated HCN (1–0) and HCO^+ (1–0) emission do not appear to have a simple interpretation, in terms of the AGN dominance or the star formation rate, and are likely determined by multiple processes, including density and radiative effects.

Subject headings: galaxies: ISM — galaxies: starburst — galaxies: active

1. INTRODUCTION

Molecular gas is observationally linked to ongoing star formation through observed correlations between the star formation rate surface density and the H_2 surface density as inferred from CO observations (e.g., Bigiel et al. 2008; Leroy et al. 2012). CO (1–0) has a relatively low critical density ($n_{crit} \approx 2 \times 10^3$ cm^{-3}) and so traces the bulk of the molecular gas. Molecular transitions such as HCN (1–0) and HCO^+ (1–0) have critical densities $n_{crit} \approx 3 \times 10^6$ cm^{-3} and 2×10^5 cm^{-3}, respectively, at 30 K, and so they are associated with higher density molecular hydrogen. Early studies found a linear correlation between HCN (1–0) and the infrared luminosity—$L_{IR}[8-1000\ \mu m]$—of galaxies (Solomon et al. 1992; Gao & Solomon 2004b). This relation, which is tighter than that for CO (1–0) with L_{IR}, was interpreted as evidence that HCN (1–0) traces the dense gas directly associated with star formation. Revisiting the relationship between SFR and this molecular tracer, García-Burillo et al. (2012) find L_{FIR} to be a super-linear function of HCN (1–0), suggesting that there are other physical factors that are important for the HCN emission.

Calling into question the use of HCN (1–0) as a tracer of dense gas, several studies of systems hosting active galactic nuclei (AGN) have found integrated (Graciá-Carpio et al. 2006; Krips et al. 2008) and spatially-resolved enhancements (Kohno et al. 2003; Imanishi et al. 2006, 2007, 2009; Davies et al. 2012) of HCN (1–0) emission compared to what is observed in starburst galaxies. Similar results have been found for HCN (4–3) (Iman-

gprivon@astro-udec.cl

[1] Based on observations carried out with the IRAM 30m Telescope. IRAM is supported by INSU/CNRS (France), MPG (Germany) and IGN (Spain).

[2] Department of Astronomy, University of Virginia, Charlottesville, VA, USA
[3] Departamento de Astronomía, Universidad de Concepción, Concepción, Chile
[4] Visiting Graduate Student Research Fellow (2013), NASA Infrared Processing and Analysis Center, California Institute of Technology, Pasadena, CA, USA
[5] Instituto de Astrofísica de Andalucíaa-CSIC, Glorieta de la Astronomía s/n, 18008, Granada, Spain
[6] National Radio Astronomy Observatory, Charlottesville, VA, USA
[7] ICREA and Institut de Ciències del Cosmos (ICC), Universitat de Barcelona (IEEC-UB), Martí i Franquès 1, 08028, Barcelona, Spain
[8] Spitzer Science Center, California Institute of Technology, Pasadena, CA, USA
[9] Universidad Diego Portales, Chile
[10] Infrared Processing and Analysis Center, California Institute of Technology, Pasadena, CA, USA
[11] Chalmers University of Technology, Department of Earth and Space Sciences, Onsala Space Observatory, 43992 Onsala, Sweden
[12] National Radio Astronomy Observatory, Green Bank, WV, USA
[13] National Optical Astronomy Observatory, 950 North Cherry Avenue, Tucson, AZ 85719, USA
[14] The SETI Institute, 189 Bernardo Ave, Suite 100, Mountain View, CA 94043, USA

ishi & Nakanishi 2013, 2014). These results suggest that HCN emission is enhanced in the presence of AGN, potentially invalidating the use of HCN as a tracer of the dense molecular gas associated with ongoing star formation, particularly in systems with AGN. However it is notable that some systems with a known AGN do not show this enhanced ratio (ARP 299, Imanishi & Nakanishi 2006; I Zw 1, Evans et al. 2006), suggesting the HCN (1–0) emission enhancement observed in some AGN hosts may have a more nuanced interpretation.

Modeling by various authors suggests the HCN and HCO^+ emission are affected by density, radiative, and abundance/ionization effects which potentially complicates interpretation of the line ratios in both photon dominated and X-ray dominated regions (PDR and XDR, respectively; e.g., Aalto et al. 1994, 1995; Huettemeister et al. 1995; Lepp & Dalgarno 1996; Meijerink et al. 2007). The possible influence of the XDR on molecular abundances has been used to argue that elevated HCN (1–0) is a signpost of an AGN, however Juneau et al. (2009) and Costagliola et al. (2011) argue the excitation of HCN and HCO^+ is not solely driven by abundance and so this ratio may not solely trace XDRs. The relative influence of the other effects (infrared pumping, source compactness) has not been fully established.

In order to investigate the relation between the presence and strength of an AGN, and the HCN and HCO^+ emission in a large sample of gas-rich galaxies, we have observed 58 luminous and ultraluminous infrared galaxies ((U)LIRGs; $L_{IR} > 10^{11}$ $L_\odot$), selected from the Great Observatories All-sky LIRG Survey (GOALS; Armus et al. 2009), with the Institut de Radioastronomie Millimétrique (IRAM) 30m Eight Mixer Receiver (EMIR; Carter et al. 2012). These new observations (Section 2) of the molecular rotational transitions, HCN (1–0) and HCO^+ (1–0), are used in combination with calibrated AGN strengths determined from Spitzer/IRS (Houck et al. 2004) spectroscopy of the GOALS sample (Stierwalt et al. 2013; Inami et al. 2013) to assess the correlation of AGN strength with the global HCN (1–0) and HCO^+ (1–0) emission (Section 3). We then discuss the possible explanations for enhanced HCN (1–0) (Section 4). Finally, we explore the utility of HCN (1–0) and HCO^+ (1–0) as tracers of the mass of dense gas associated with star formation (Section 5).

The power of this study comes from the increased sample size of (U)LIRGs with measurements of these lines and, particularly, from the large number of sources with measured mid-infrared diagnostic of the relative contributions of AGN and star formation to the infrared luminosity of each system (a factor of 4 increase over Costagliola et al. 2011). The use of the mid-infrared diagnostics facilitates a good estimation of the importance of an AGN to the mid-infrared emission (i.e., as opposed to simply using rudimentary optical "AGN" and "starburst" diagnostics to classify systems). This enables a direct investigation of the global $L'_{HCN\ (1-0)}/L'_{HCO^+\ (1-0)}$ line ratio (hereafter, HCN/HCO^+) as a function of the contribution of the AGN to the bolometric luminosity.

Throughout the paper we adopt a WMAP-5 cosmology (Hinshaw et al. 2009, $H_0 = 70$ km s^{-1} Mpc^{-1}, $\Omega_{vacuum} = 0.72$, $\Omega_{matter} = 0.28$), with velocities corrected for the 3-attractor model of Mould et al. (2000).

2. SAMPLE, OBSERVATIONS, AND DATA

2.1. *GOALS*

As noted, the data presented here were obtained as part of a millimeter survey of (U)LIRGs selected from GOALS. The GOALS sample as a whole consists of all the (U)LIRGs from the Revised Bright Galaxy Sample (RBGS; i.e., 60 μm flux density greater than 5.24 Jy and $L_{IR} > 10^{11}$ $L_\odot$; Sanders et al. 2003). GOALS[15] is a multi-wavelength survey aimed at understanding the physical conditions and activity in the most luminous galaxies in the local Universe. The dataset includes spectroscopic and imaging observations in the infrared from Spitzer (Petric et al. 2011; Inami et al. 2013; Stierwalt et al. 2013, J. M. Mazzarella et al. *in prep*) and Herschel (Diaz-Santos et al. 2013, 2014; Lu et al. 2014), GALEX and HST UV, optical, and near-infrared imaging (Howell et al. 2010; Haan et al. 2011; Kim et al. 2013, A. S. Evans et al. *in prep*), Chandra X-ray observations (Iwasawa et al. 2011), and a suite of ground-based radio and sub-millimeter observations (e.g., Leroy et al. 2011; Barcos-Muñoz et al. 2015, Herrero-Illana et al. *in prep*). These observations collectively trace the obscured and unobscured activity and constrain the structural properties and merger stages of these systems.

The objects in this study were selected from two portions of GOALS; a high-luminosity sample ($L_{IR} \geq 10^{11.4}$ $L_\odot$) to capture the most extreme star forming systems, and a sample of LIRGs with $L_{IR} \leq 10^{11.4}$ $L_\odot$ which were selected to be isolated or non-interacting, on the basis of their stellar morphology (Stierwalt et al. 2013). The combination of these subsets of GOALS ensures this sample spans the range of L_{IR} and merger stage within the GOALS sample as a whole.

2.2. *Observations and Data Reduction*

The IRAM 30m Telescope was used with the EMIR receiver to observe an 8 GHz instantaneous bandwidth, tuned to simultaneously capture HCN ($J = 1 \rightarrow 0$), HCO^+ ($J = 1 \rightarrow 0$), the CCH ($N = 1 \rightarrow 0$) multiplet, and HNC ($J = 1 \rightarrow 0$), thus reducing systematic uncertainties when comparing the fluxes of these lines. The rest frequencies[16] for these transitions are: ν_{rest}(HCN (1–0)) = 88.631 GHz, ν_{rest}(HCO^+ (1–0)) = 89.189 GHz, and ν_{rest}(HNC (1–0)) = 90.663 GHz. For CCH, we adopt a rest frequency which is the simple arithmetic mean of the individual multiplet frequencies, ν_{rest}(CCH) = 87.370 GHz. The beam FWHM for these measurements is ~ 28", corresponding to a linear size of 16.8 kpc at the mean redshift of our sample – thus we obtain galaxy-integrated measurements. Observations were done in wobbler switching mode ($\sim 1'$ throw, 0.8 s switching) to improve the baseline calibration. In Table 1 we list the pointing coordinates, assumed redshift, observing year & month, integration times, system temperatures, and the backend used, for each source.

Some of our observations use the FTS backend, which consists of 24 individual fourier transform spectrometer units. In some scans, the FTS units exhibited gain variations, resulting in offsets of the baselines for individual

[15] http://goals.ipac.caltech.edu

[16] obtained from the Splatalogue database: http://splatalogue.net

units. For those scans, linear fits were made to the baseline of each unit (masking out the expected locations of spectral lines), and the units were corrected to a common baseline. Scans were combined and exported using the GILDAS/CLASS software[17]. Further analysis, including a linear baseline subtraction, smoothing, and flux measurement, was done using the *pyspeckit* software[18] (Ginsburg & Mirocha 2011). The typical velocity resolution of these smoothed data is 60 MHz, corresponding to roughly 215 km s^{-1}. In Figure 1 we show the reduced spectra for all sources, with the expected positions of the CCH, HCN (1–0), HCO$^+$ (1–0), and HNC (1–0) lines marked. Lines were identified visually based on cataloged optical redshifts and total fluxes were determined by integrating under the line. IRAS F16164-0746 had spectra which were clearly shifted from the location expected based on the cataloged redshift. We measured a new redshift of 0.0229 for IRAS F16164-0746 compared to the value from NED, 0.0272.

We determined uncertainties in the fluxes by calculating the RMS, σ_{ch}, per channel of width dv, in the line-free regions of the spectrum and multiplying by the square root of the number of channels, N_{ch} covered by each line. We considered a line a detection if the measured flux exceeded $3\sigma_{ch}dv\sqrt{N_{ch}}$. For non-detections we calculated a 3σ upper limit by assuming a square line profile with a width half that of the detected HCN (1–0) or HCO$^+$ (1–0) line, or 200 km s^{-1} if no lines were detected for that source.

For IRAM 30m observations, temperatures are reported on the T_A^* scale; these values were converted to a main beam temperature, $T_{mb} = T_A^*/(B_{eff}/F_{eff})$ using the main beam efficiency, $B_{eff} = 0.81$, and a forward efficiency, $F_{eff} = 0.95$, both measured by IRAM staff on 26 August 2013[19]. We use a Jy/K conversion of $3.906(F_{eff}/A_{eff}) = 6.185$, where $A_{eff} = 0.6$, to convert the reported T_A^* values to flux densities. Line luminosities were computed according to Solomon et al. (1992, their Equation 3), in units of K km s^{-1} pc^2.

As noted, the wide EMIR bandwidth enables simultaneous measurements of HCN (1–0), HCO$^+$ (1–0), HNC (1–0), and CCH. We had a detection rate of 78%, 76%, 35%, and 37%, for HCN (1–0), HCO$^+$ (1–0), HNC (1–0), and CCH, respectively. For detected lines the signal-to-noise weighted mean HNC (1–0)/HCN (1–0) and CCH/HCN (1–0) ratios are 0.5 ± 0.3 and 0.8 ± 0.3, respectively. One source, NGC 6285 has detected CCH emission and no detection of HCN (1–0) or HCO$^+$ (1–0); the CCH detection is $\sim 3.8\sigma$ and, if confirmed, would be an interesting and rare example of a source with CCH brighter than HCN or HCO$^+$. Such elevated CCH emission may indicate an overabundance of CCH or a lack of dense molecular gas (Martín et al. 2014). The HCN (1–0)/HCO$^+$ (1–0) ratio is discussed in more detail in Section 3. Integrated fluxes (or 3σ upper limits) are provided for all lines, in Table 2, but we limit the analysis here to the HCN (1–0) and HCO$^+$ (1–0) lines. Upper and lower limits in Figures use these 3σ limits. CO (1–0) observations were also obtained as part of this program; these will be presented in R. Herrero-Illana et al. (*in prep*).

In order to explore the influence of AGN on the HCN (1–0) and HCO$^+$ (1–0) emission, we use the equivalent width (EQW) of the 6.2 μm polycyclic aromatic hydrocarbon (PAH) measured from Spitzer/IRS low-resolution observations (Stierwalt et al. 2013). The EQW of the 6.2 μm PAH feature compares the strength of the PAH emission associated with star formation with the strength of the mid-infrared continuum (e.g., Genzel et al. 1998; Armus et al. 2004, 2007). The AGN is energetically more important in systems with lower values of the PAH EQW. Points in Figures 2–7 are color-coded by their 6.2 μm PAH EQW, to show the relationship between AGN and starburst dominated systems.

In addition to our new measurements, we incorporate observations from Graciá-Carpio et al. (2006), Costagliola et al. (2011), and García-Burillo et al. (2012) in our analysis. The combination of these three samples includes 63 individual galaxies with measured 6.2 μm PAH EQWs and detections in at least one of HCN (1–0) or HCO$^+$ (1–0), comprising roughly 25% of the objects in the GOALS sample.

We use L_{IR} measurements from IRAS observations (Armus et al. 2009). For galaxies in pairs, we assign a portion of L_{IR} to each component based on their 70 or 24 μm flux ratio, as described by Diaz-Santos et al. (2013). Measurements of the [C II] 158 μm line are taken from Diaz-Santos et al. (2013).

2.2.1. *Comparison with Previous Measurements*

Several of the sources observed by us have pre-existing published fluxes in the literature (e.g., Gao & Solomon 2004a; Graciá-Carpio et al. 2006; García-Burillo et al. 2012). We compared our fluxes with those previous efforts and found good agreement for some sources (e.g., ARP 220, VV 114, NGC 0034, IRAS 15107+0724, IRAS 23365+3604), but we measure fluxes for some individual sources (NGC 2623, NGC 6701, UGC 5101, and NGC 7591) which are factors of $2-3$ higher than those previously published. There appears to be no trend of these high fluxes with observing date or observing setup. Despite some differences in fluxes for some sources, we find the HCN/HCO$^+$ ratios for those sources are in good agreement with previously published ratios.

2.3. *Distance and Aperture Effects*

2.3.1. *Source Distance Effects*

The 28″ IRAM 30m beam FWHM covers linear scales of $6.1-46$ kpc for these sources. Thus, these single-dish observations average together emission from many giant molecular clouds (GMCs) within each system, likely with varying physical conditions and environments. This factor of ~ 8 in distance leads to possible concerns about the effects of beam size on the results, particularly if there are systematic variations in the GMC properties or environments as a function of distance from the nuclei.

Previous interferometric observations with $\sim 5''$ resolution have found the HCN (1–0) and HCO$^+$ (1–0) emission to be unresolved in ULIRGs (Imanishi et al. 2007, 2009). For the sources from their study that overlap with our sample, we find general agreement between the fluxes, suggesting the amount of extended flux is minimal and the HCN and HCO$^+$ emission is confined to a

[17] http://www.iram.fr/IRAMFR/GILDAS
[18] http://pyspeckit.bitbucket.org
[19] http://www.iram.es/IRAMES/mainWiki/Iram30mEfficiencies

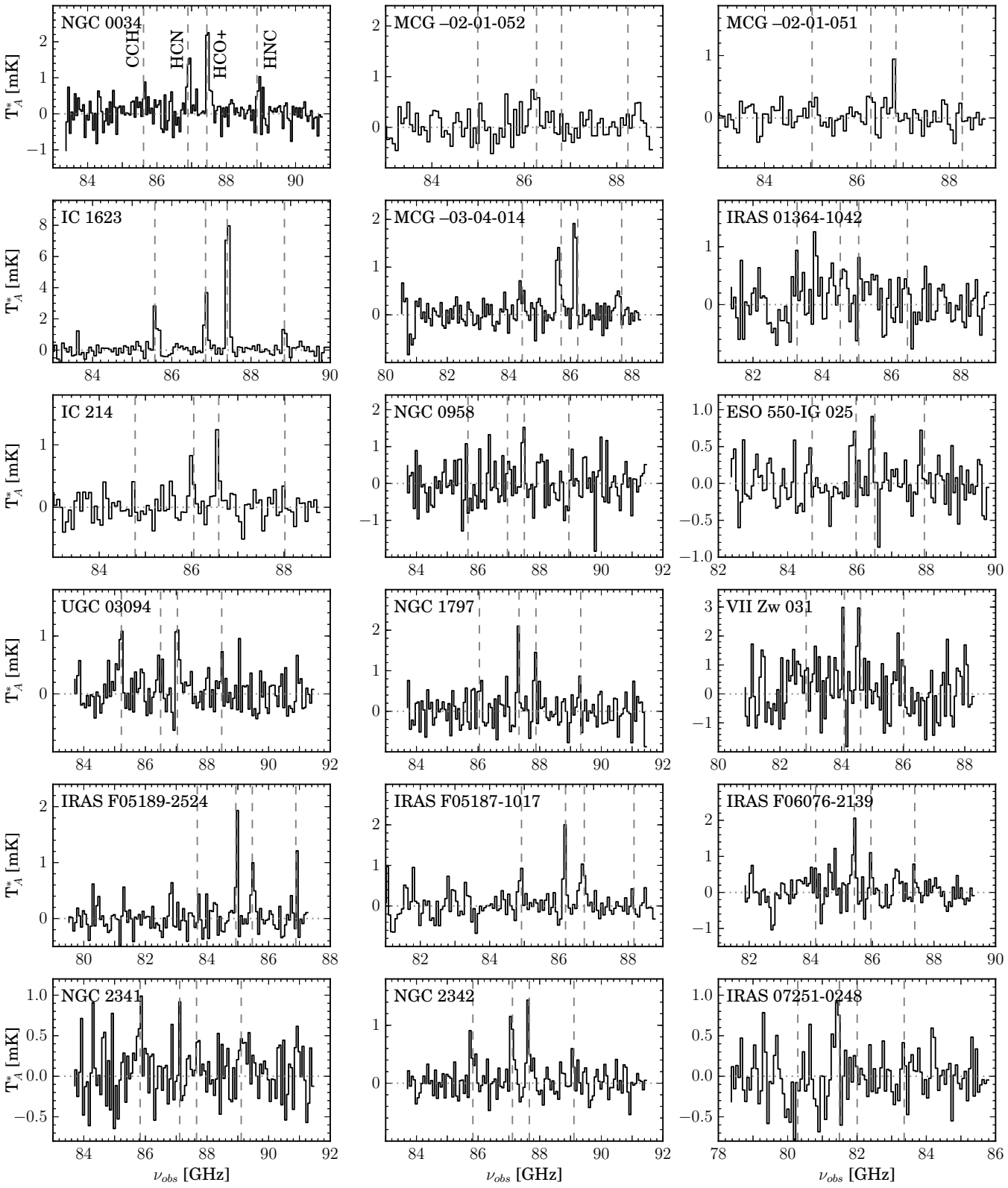

Figure 1. IRAM 30m EMIR spectra of the systems observed as part of this program, sorted by Right Ascension. In all panels we plot the observed T_A^* as a function of the observed frequency. The typical velocity resolution of these smoothed data is 60 MHz, corresponding to roughly 215 km s^{-1}. Dashed vertical lines mark (from left to right) the expected locations of CCH, HCN (1–0), HCO$^+$ (1–0), and HNC (1–0), based on optical redshifts from NED, except for IRAS F16164-0746, where we have used our new measured redshift. Information on the observing parameters are provided in Table 1. Integrated fluxes (or upper limits) for each line are given in Table 2. *This figure is continued at the end of the manuscript, in the Figures currently labeled 8–10.*

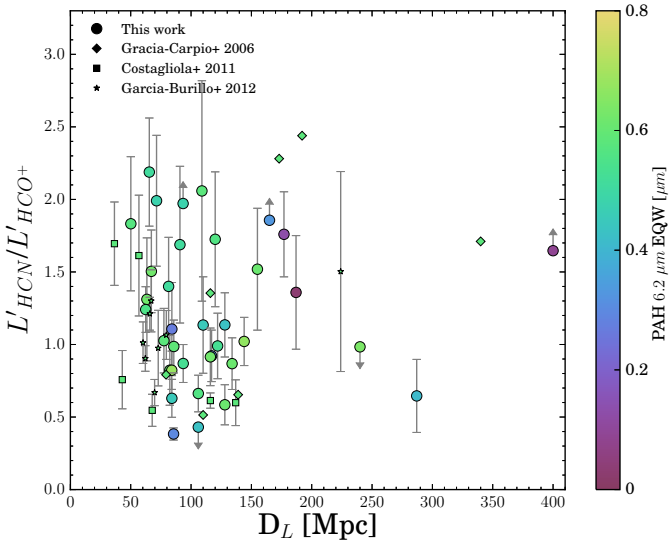

Figure 2. Ratio of the $L'_{HCN\ (1–0)}$ and $L'_{HCO^+\ (1–0)}$ luminosities versus luminosity distance. The lack of a significant correlation suggests our results are not being affected by the distances to each system. Points are color-coded by the 6.2 μm PAH EQW.

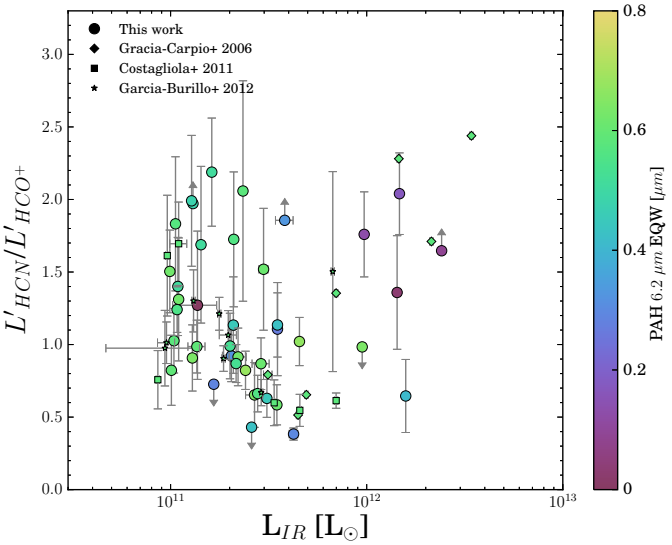

Figure 3. Ratio of $L'_{HCN\ (1–0)}$ to $L'_{HCO^+\ (1–0)}$ luminosities versus the total infrared luminosity. Points are color-coded by the 6.2 μm PAH EQW.

region smaller than the 28″ beam of these IRAM 30m observations.

In Figure 2 we compare the HCN/HCO$^+$ ratio with the luminosity distance; there is no obvious trend with distance, suggesting that the projected beam size is not the dominant factor in determining the HCN/HCO$^+$ ratio in our sample.

2.3.2. *Spitzer vs IRAM 30m Telescope Aperture Comparison*

The 6.2 μm PAH EQW used to assess the relative dominance of the AGN in the mid-infrared was measured from a 3.6″ aperture (Stierwalt et al. 2013). Thus, these measurements are upper limits to the large-scale influence of the AGN, and we expect any systematic effect of this aperture difference between the mid-infrared and millimeter observations would serve to overestimate the importance of the AGN.

In other words, we would expect any signature of AGN-dominated gas to be diluted with increasing source distance. As will we shown (Section 3), the excitation of these molecular transitions does not appear to be solely a function of the AGN strength, thus we conclude our results are not being significantly biased by the mis-match in aperture between the millimeter and mid-infrared datasets.

3. ENHANCED GLOBAL HCN (1–0) EMISSION DOES NOT UNIQUELY TRACE AGN ACTIVITY

Some of the initial claims that HCN (1–0) is enhanced in AGN were supported by plotting the $L'_{HCN\ (1–0)}/L'_{CO\ (1–0)}$ and $L'_{HCO^+\ (1–0)}/L'_{CO\ (1–0)}$ ratios as a function of L_{IR}. In Figure 3 we show the HCN (1–0)/HCO$^+$ (1–0) ratio as a function of L_{IR}[20], to compare we previous work. As in previous studies (e.g., Graciá-Carpio et al. 2006), we find a relative dearth of sources at high L_{IR} with low HCN/HCO$^+$.

However, our larger sample also contains a number of lower L_{IR} systems with HCN/HCO$^+$ ratios as high as those of ULIRGs (> 1), which suggests that increasing L_{IR} (or an associated increase in AGN contribution) may not be the sole driver of an increase in HCN/HCO$^+$ ratios. A Spearman rank correlation analysis is consistent with the null hypothesis that HCN/HCO$^+$ and L_{IR} are uncorrelated ($\rho = 0.021 \pm 0.178$, z-score$= 0.057 \pm 0.494$; Table 3). The coefficients were computed using a Monte Carlo perturbation and bootstrapping method (with 10^5 iterations), as described by Curran (2014) and implemented in Curran (2015).

The Spitzer/IRS observations of GOALS systems, presented by Stierwalt et al. (2013), provide a calibrated measurement of the AGN contribution to the mid-infrared emission in each system, via the 6.2 μm PAH EQW. In order to test claims that HCN (1–0) emission is enhanced in systems with AGN, we explore the HCN/HCO$^+$ ratio as a function of this AGN diagnostic. In Figure 4 (Left), we plot HCN/HCO$^+$ against the relative contribution of AGN and star formation to the infrared luminosity; where lower values of the PAH EQW indicate the presence of more energetically important AGN. We consider systems with PAH EQW < 0.2 μm to have energetically dominant AGN ($L_{MIR,AGN}/L_{MIR} \gtrsim 60$ %;) e.g., Petric et al. 2011), while systems with PAH EQW > 0.55 μm are considered starburst-dominated (Brandl et al. 2006), and systems with intermediate ratios as composites, where L_{MIR} is the mid-infrared luminosity and $L_{MIR,AGN}$ is the AGN contribution to the mid-infrared luminosity.

We find that systems dominated by the AGN in the mid-infrared show elevated HCN/HCO$^+$ ratios, with a signal-to-noise ratio weighted mean ratio of 1.84 ± 0.43.

[20] Here we do not compare with CO (1–0) as this would potentially include molecular gas which is not physically associated with the regions emitting in HCN (1–0) and HCO$^+$ (1–0). For this study, we rely on the HCN/HCO$^+$ ratio alone, to avoid concerns with mis-matched apertures between the CO (1–0) measurements and the HCN (1–0) and HCO$^+$ (1–0) (a 30% difference in beam size).

Starburst dominated systems have a weighted mean ratio of 0.88 ± 0.28, while composite systems have a weighted mean ratio of 1.14 ± 0.49. However, for systems which appear to be star formation dominated, this ratio exhibits significant scatter. Several starburst and composite systems have HCN/HCO$^+$ values which are comparable to the AGN dominated systems, suggesting that while energetically dominant AGN are associated with elevated HCN (1–0) emission alone, the converse is not true: enhanced HCN (1–0) emission does not imply the presence of an AGN. We note that although these starburst and composite sources with enhanced HCN (1–0) emission have substantial uncertainties in their HCN/HCO$^+$ ratios, it is unlikely that the HCN/HCO$^+$ ratio is simultaneously overestimated for all six of these HCN-enhanced, composite/starburst sources.

A Spearman rank correlation analysis shows HCN/HCO$^+$ and the PAH EQW to be moderately anti-correlated, with $\rho = -0.512 \pm 0.127$ and a z-score of -1.532 ± 0.464 (Table 3). In Figure 4 (Right) we provide a "box plot" of the mean ratio, interquartile range, and full range of the HCN/HCO$^+$ values, separated by into source types based on the PAH EQW. The distributions of HCN/HCO$^+$ for pure starbursts and AGN-dominated systems show a clear offset, with the AGN-dominated systems show a relative enhancement of HCN (1–0) emission over the pure starbursts.

It is worth noting there are fewer AGN-dominated sources than SB or composite sources; further observations of low PAH EQW systems would be useful to ensure the existing objects are representative.

4. WHAT DRIVES THE GLOBAL HCN (1–0)/HCO$^+$ (1–0) RATIO?

In Section 3 we demonstrated that globally enhanced HCN (1–0) emission (relative to HCO$^+$ (1–0)) is not correlated with the presence of an AGN (Figure 4). Costagliola et al. (2011) found similar results for a smaller sample of starbursts. Is there a straight-forward explanation for the observed global HCN (1–0) emission in local (U)LIRGs? In the following subsections we explore a series of proposed explanations for enhanced HCN, including X-ray induced chemistry (Section 4.1), the presence of a compact, high-density source (Section 4.2), and radiative pumping from absorption of mid-infrared photons (Section 4.3). We finish by discussing the possibility that the PAH EQW is not an ideal tracer of AGN (Section 4.4) and then mention future observations which could be used to improve our understanding of HCN enhancements (Section 4.5).

4.1. *Comparison of HCN (1–0)/HCO$^+$ (1–0) with X-ray Properties*

To consider the possible influence of XDRs resulting from powerful AGN, we investigated the HCN/HCO$^+$ ratio as a function of X-ray properties, such as the hardness ratio and the total 0.5–10 keV X-ray luminosity, from Chandra X-ray observations of the GOALS sample (Iwasawa et al. 2011). The HCN/HCO$^+$ ratio showed no correlation with either the hardness ratio or the X-ray luminosity, albeit with only ten sources common to both samples. Additional X-ray observations would be useful to further investigate the influence of XDRs. However, based on the currently available X-ray data, it does not appear that either the hardness of the X-ray spectrum or the total X-ray luminosity correlate with HCN/HCO$^+$, suggesting an XDR is not generally a major driver in enhancing HCN (1–0), for these systems, possibly because the XDRs are spatially disconnected from the regions that dominate the global line luminosity.

A complication is that enhancement from X-rays may be most effective in obscured AGN and diagnosing this activity is difficult with observations below 10 keV. Hard X-ray observations with NuSTAR (Harrison et al. 2013), though time-consuming, would provide an interesting test for the presence of obscured AGN in sources with enhanced HCN emission.

4.2. *HCN/HCO$^+$ Enhancements Through Source Compactness*

In compact environments HCO$^+$ (1–0) appears to be more susceptible to self-absorption than HCN (1–0) (Aalto et al. 2015), which would lead to an increase in the observed HCN/HCO$^+$ ratio. To test if elevated ratios are primarily associated with dense systems, we compare, in Figure 5, the HCN/HCO$^+$ ratio with the [C II]/L$_{\rm FIR}$ ratios from the central Herschel spaxel ($9''.4 \times 9''.4$) as measured by Diaz-Santos et al. (2013). In local galaxies, the [C II]/L$_{\rm FIR}$ value decreases with increasing L$_{\rm FIR}$ and dust temperature, T$_{dust}$. That the "[C II] deficit" tracks T$_{dust}$ suggests the deficit is the result of compact nuclear activity. Diaz-Santos et al. (2013) find this trend of a lower [C II]/L$_{\rm FIR}$ ratio with decreasing source size is present when considering only starbursts, suggesting that the [C II] deficit is driven by the compactness of the starburst, rather than dust heated by an AGN.

Therefore, if the HCN (1–0)/HCO$^+$ (1–0) ratio is being driven primarily by the density / compactness of the starburst, we should see a correlation between the two quantities. For sources with [C II]/L$_{\rm FIR}$ $> 10^{-3}$, the signal-to-noise weighted mean L$'_{\rm HCN\ (1–0)}$ to L$'_{\rm HCO^+\ (1–0)}$ is 1.0 ± 0.4, while sources with [C II]/L$_{\rm FIR}$ $< 10^{-3}$ (large [C II] deficits) have a mean ratio of 1.7 ± 0.5. Formally, the ratio does not appear to vary as a function of [C II]/L$_{\rm FIR}$ though a Spearman rank analysis suggests a moderate anti-correlation ($\rho = -0.401 \pm 0.142$, z-score$= -1.165 \pm 0.458$; Table 3), though somewhat weaker than the anti-correlation of HCN/HCO$^+$ with PAH EQW. The majority of sources with [C II]/L$_{\rm FIR}$ $< 10^{-3}$ have HCN/HCO$^+$ ratios > 1, consistent with a scenario in which a compact and dense starburst causes an enhancement of HCN (1–0). On the other hand, a substantial number of systems without significant [C II]/L$_{\rm FIR}$ deficits also have HCN/HCO$^+$ > 1. For composite and starburst systems (PAH EQW $> 0.2\ \mu m$) higher HCN/HCO$^+$ ratios do not appear to be associated with lower [C II]/L$_{\rm FIR}$ values. Based on the available data, we cannot directly link the [C II] deficit with enhanced HCN (1–0) emission.

It is worth noting that HCN (1–0) can be enhanced in sources that do not show a strong [C II] deficit; if a compact continuum source is surrounded by extended disk-like star formation, the system may have a "normal" [C II]/L$_{\rm FIR}$ ratio, but still show enhanced HCN (1–0) associated with the compact starburst on scales which cannot be resolved by Herschel. See Diaz-Santos et al. (2014) for a discussion on extended [C II] emission in the GOALS sample. Assessing the spatial distribution of the

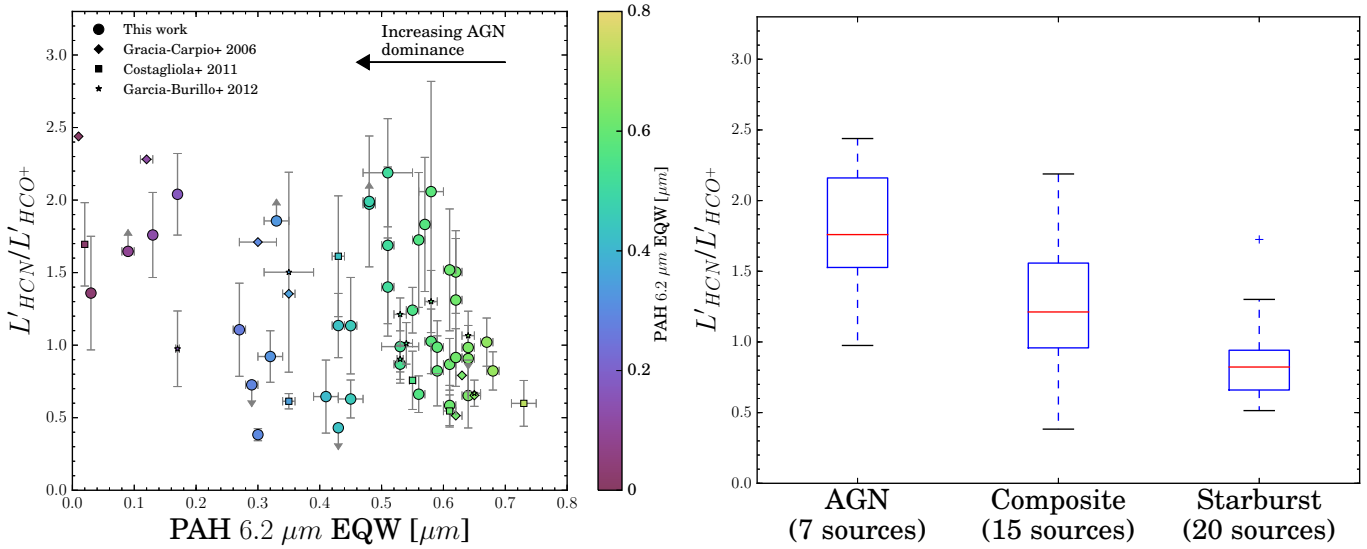

Figure 4. Left: $L'_{HCN\ (1-0)}/L'_{HCO^+\ (1-0)}$ as a function of the 6.2 μm PAH EQW from Stierwalt et al. (2013). The points are colored by their PAH EQW. The symbol shape notes the origin of the millimeter line measurements; circles are new data (see Table 2), diamonds are from Graciá-Carpio et al. (2006) and squares are from Costagliola et al. (2011). Right: Box plot showing the median (red line), interquartile range (boxes) and full range up to 1.5× the interquartile range (IQR; black horizontal lines) for HCN/HCO$^+$ of the AGN dominated, composite, and starburst systems. A flier (a point with a value > 1.5 × IQR) is plotted with a '+' symbol. Upper and lower limits were not included in the box plot. HCN/HCO$^+$ is enhanced for systems which are AGN dominated in the mid-infrared, but some starburst dominated systems show similarly elevated ratios. Weighted by signal-to-noise ratio, the average ratio for AGN dominated systems (PAH EQW < 0.2 μm), pure starbursts (PAH EQW > 0.55 μm Brandl et al. 2006), and composite systems (0.2 μm < PAH EQW < 0.55 μm) is 1.84, 0.88, and 1.14, respectively.

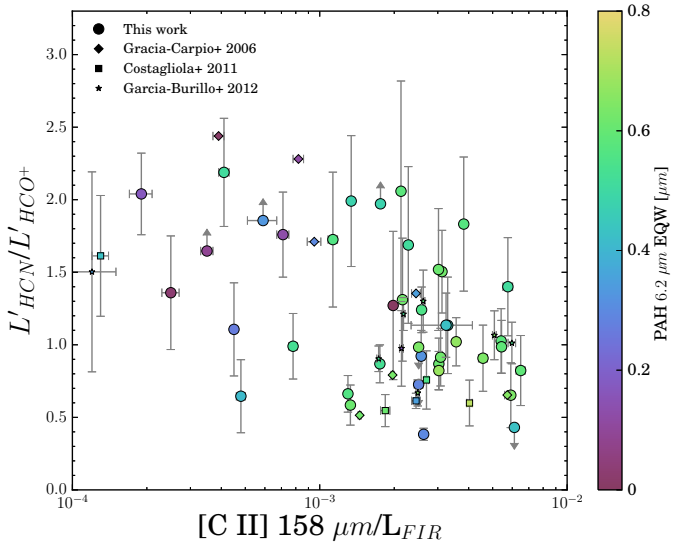

Figure 5. A comparison of HCN/HCO$^+$ with [C II]/L_{FIR}, as a proxy for the compactness of the source. Systems with significant [C II] deficits are located towards the left side of the plot. There is a dearth of sources with low [C II]/L_{FIR} values and low HCN/HCO$^+$ ratios, but the scatter is significant and some systems with high [C II]/L_{FIR} values (less compact starbursts) still show elevated HCN/HCO$^+$ ratios, consistent with the mean of systems with substantial deficits ([C II]/L_{FIR} < 10^{-3}). However there is significant scatter. Points are color-coded by the 6.2 μm PAH EQW.

HCN (1–0)/HCO$^+$ (1–0) would be a useful comparison with [C II]/L_{FIR}– do regions with "normal" [C II]/L_{FIR} correspond to regions with low HCN (1–0)/HCO$^+$ (1–0)?

A possible concern with the above analysis is that the L_{IR}, [C II]/L_{FIR}, and the PAH EQW are all correlated. Indeed, the L_{IR}, the [C II] deficit, and the 6.2 μm PAH EQW are interrelated, in that the most luminous sources tend to have the strongest [C II] deficits (Diaz-Santos et al. 2013, because both L_{IR} and [C II]/L_{FIR} correlate with the dust temperature;) and lower PAH EQWs (Petric et al. 2011; Stierwalt et al. 2013). However, the converse is not true; a normal [C II]/L_{FIR} value does not guarantee a high PAH EQW. Systems with low or intermediate PAH EQWs are distributed across the range of L_{IR} and [C II]/L_{FIR} values seen for our sample (e.g., Figure 5 and Diaz-Santos et al. 2013).. In contrast, essentially all the high PAH EQW (starburst) systems have normal [C II]/L_{FIR} and L_{IR} ∼ a few ×10^{11} $L_\odot$. Thus, while these quantities are generally related, systems with low or intermediate PAH equivalent widths appear to have a range of compactness (as diagnosed by [C II]/L_{FIR}) and so the PAH EQW and [C II] deficit appear to be semi-independent. That the HCN (1–0)/HCO$^+$ (1–0) ratio does not correlate well with either, suggests the origin of HCN enhancement cannot be easily assigned solely to AGN or to the presence of a compact starburst.

4.3. *HCN/HCO$^+$ Enhancements Through Mid-infrared Pumping*

The strong mid-infrared continuum present in many (U)LIRGs may also influence these line ratios. The HCN molecule has degenerate bending modes in the infrared and can absorb mid-infrared photons (14 μm) to its first vibrational state. The transitions have high level energies (> 1000 K) and mid-IR emission with a brightness temperature of at least 100 K is necessary to excite them (Aalto et al. 2007). A sign that infrared pumping of HCN is taking place is the presence of line emission from rotational transitions within the vibrational band (e.g.,

Sakamoto et al. 2010). However, it may be possible for HCN to be infrared pumped without detectable emission from these rotational-vibrational lines. When the brightness temperature is close to the lower limit for pumping, the excitation of the rotational-vibrational line is so low that it takes a very large column density to result in a large enough optical depth for this rotational-vibrational line to be detected.

Several sources in our sample do show evidence for infrared absorption at 14 μm which could be associated with pumping of HCN (Lahuis et al. 2007; Sakamoto et al. 2010), but none of the starburst systems with enhanced HCN emission show 14 μm absorption in the Spitzer/IRS observations from Inami et al. (2013).

HCO^+ is similarly susceptible to infrared pumping, via a $\sim$ 12 μm line; using the IRS high-resolution spectroscopy from Inami et al. (2013) we searched for a $\sim$ 12 μm absorption feature in those systems with high ratios, where we postulated mid-infrared pumping could be important. We did not find any evidence for HCO^+ absorption.

However, it is not clear that existing mid-infrared observations are sensitive enough to establish firm upper limits on the importance of infrared pumping. Existing spectroscopy may not have the sensitivity to identify absorption which is sufficient to affect level populations.

4.4. *Is the PAH EQW A Good Tracer of AGN Strength*

An obvious question is whether or not the PAH EQW is a robust measure of AGN strength in (U)LIRGs. Aalto et al. (2015) present interferometric observations of several objects, including the composite source CGCG 049-057, one of our sources with enhanced HCN emission. The HCN (3–2) $v_2 = 0$ and HCO^+ (3–2) lines show evidence for significant self absorption and the HCN (3–2) $v_2 = 1$ ro-vibrational line is detected (consistent with mid-infrared pumping). Aalto et al. (2015) interpret this as evidence for a very compact (tens of pc) warm (> 100 K) region surrounded by a large envelope of cooler, more diffuse gas. The total column density through these systems is likely quite high ($> 10^{24}$ cm^{-2}). If the column densities are sufficiently high to support mid-infrared pumping, the optical depths in the infrared may be high enough that the mid-infrared continuum level does not trace the intrinsic energy source – thus the PAH EQW diagnostic may miss highly embedded AGN.

In Section 2.3.2 we note that the PAH EQW is an upper limit to the AGN's influence on large scales, but this measurement could also be considered as a lower limit to the AGN's influence on smaller scales. Thus, consistent with results of Aalto et al. (2015) for CGCG 047-059, it is possible that these starburst or composite sources with high HCN (1–0)/HCO^+ (1–0) ratios host embedded AGN, and substantial mid-infrared optical depths result in an under-estimate of the AGN's influence when using the PAH EQW.

4.5. *Future Observations*

Though we have shown in this study that some starburst-dominated systems have global $L'_{\rm HCN\ (1–0)}/L'_{\rm HCO^+\ (1–0)}$ ratios in excess of unity, the starburst-dominated systems outnumber AGN-dominated systems in the present sample. More IRAM 30m single-dish observations of AGN-dominated (U)LIRGs would be useful to study the dense-gas tracers in that population, particularly to see if the absence of AGN-dominated sources with low $L'_{\rm HCN\ (1–0)}/L'_{\rm HCO^+\ (1–0)}$ ratios is truly representative or merely reflects small number statistics.

Spatially resolved comparisons of the HCN emission with CO or HCO^+ have been undertaken for systems known to host an AGN (e.g., Kohno et al. 2003; Imanishi et al. 2006, 2007, 2009; Davies et al. 2012; Imanishi & Nakanishi 2013, 2014); it would be instructive to perform the same exercise on starburst dominated systems. The Atacama Large Millimeter/sub-millimeter Array is the natural instrument for this, and such a study could investigate the spatial variation in the $L'_{\rm HCN\ (1–0)}/L'_{\rm HCO^+\ (1–0)}$ ratio for starbursts. If the ratio peaks on the nucleus but is low elsewhere (as in systems with AGN), does that correspond to a compact mid-infrared emitting region? Spatially resolving this ratio in starburst systems with both high and low ratios may enable a separation of the relative importance of source compactness and/or mid-infrared pumping, in setting the ratio.

Krips et al. (2008) studied the emission of multiple HCN and HCO^+ transitions for twelve systems, finding evidence for systematic differences in the HCN (1–0)/HCO^+ (1–0) and HCN (3–2)/HCO^+ (3–2) ratios between AGN and starbursts, with AGN having values > 2 for both ratios. They also found evidence that the (3–2)/(1–0) ratio for both HCN and HCO^+ varies between AGN and starbursts. The number of GOALS objects with (3–2) measurements of HCN and HCO^+ is currently too small to draw conclusions regarding the (3–2)/(1–0) ratios as a function of AGN strength, but it would be possibly illuminating to compare the higher J_{upper} transitions with the AGN diagnostic used here.

The discovery of mid-infrared pumping and associated high-column densities in enhanced HCN sources suggests that even mid-infrared diagnostics such as the PAH EQW may miss highly embedded AGN. If this is the case, hard X-ray observations may provide the only conclusive evidence for AGN in sources with heavily obscured nuclei. However, the weakness of the > 10 keV X-rays in ULIRG AGN (e.g., Mrk 231; Teng et al. 2014) may make these observations difficult with existing facilities.

Finally, the influence of infrared pumping is still uncertain. Future mid-infrared observations of these sources with The James Webb Space Telescope would provide tighter constraints on the importance and ubiquity of mid-infrared pumping, for both HCN and HCO^+. See also Aalto et al. (2007) for a discussion on using resolved observations to distinguish mid-infrared pumping and XDR scenarios.

5. THE RELATIONSHIPS BETWEEN MOLECULAR LINE LUMINOSITIES, STAR FORMATION RATES, AND GAS DEPLETION TIMESCALES

5.1. *Star Formation Rates*

We now turn to the relationship between the HCN (1–0) emission and the star formation rates in (U)LIRGs. While HCN (1–0) is generally taken to trace the mass of dense molecular gas, M_{dense}, previous studies have found conflicting results for the relationship between $L_{\rm IR}$ and $L'_{\rm HCN\ (1–0)}$. In Figure 6 (Left) we plot the standard re-

lation between $L'_{HCN\ (1-0)}$ and L_{IR} including additional measurements from Gao & Solomon (2004b, with values corrected to our assumed cosmology and for the 3-attractor model of Mould et al. (2000)).

We fit the relationship using a maximum likelihood technique, considering the errors in both L_{IR} and $L'_{HCN\ (1-0)}$ (e.g., Sec 7 of Hogg et al. 2010). When uncertainties for mm-line fluxes were not quoted in the literature, we assume 20%. Uncertainties on the fit parameters were determined using Markov Chain Monte Carlo (MCMC) sampling[21] and quoted fit parameter uncertainties are for the 99% confidence interval.

To this point, we have not considered systematic uncertainties in our new observations, as the simultaneous measurement of HCN and HCO$^+$ should result in significantly reduced systematic uncertainties in the HCN/HCO$^+$ ratio,in the HCN/HCO$^+$ ratio, compared to non-simultaneous measurements. However, for the present comparison of L_{IR} with these lines, the absolute flux of these lines may be subject to systematic uncertainties. We tested two approaches for dealing with systematic uncertainties: 1) assigning additional systematic uncertainties (equal in magnitude to the statistical uncertainties) to each datapoint[22] and fitting the relationship, or 2) including only statistical uncertainties[23] and allowing for additional uncertainties in the fitting process. In addition to fitting for the slope and intercept, we included an additional "nuisance" parameter, f, in the likelihood function to fit for the fractional amount by which the uncertainties are underestimated (e.g., due to not explicitly including systematic uncertainties). After the MCMC sampling, we marginalized over f when determining the final uncertainties for the slope and intercept. Both approaches yielded the same results for the best-fit relations, so we conclude that our fitting process appropriately accounts for non-statistical uncertainties and present the numerical results from the latter approach. For consistency, we show only the statistical uncertainties for values plotted in Figures 6 and 7.

Our best fit relation to our new data combined with the literature data (omitting both AGN-dominated systems, in which L_{IR} may not solely trace star formation, and HCN (1–0) upper limits) between L_{IR} and $L'_{HCN\ (1-0)}$ is:

$$\log_{10} L_{IR} = (1.08^{+0.18}_{-0.16}) \log_{10} L'_{HCN(1-0)} + (2.32^{+1.54}_{-1.50}) \quad (1)$$

This fit is shown in Figure 6 (Left) as the solid line. We also fit $L'_{HCN\ (1-0)}$–L_{IR}, fixing the slope to be linear, which we show in Figure 6 (Left) as a dashed line. The slope of the $L'_{HCN\ (1-0)}$–L_{IR} relation is consistent with being linear at the $\sim 1.3\sigma$ level. We note that García-Burillo et al. (2012) found the $L'_{HCN\ (1-0)}$–$L_{FIR}[40-400\ \mu m]$ relation to be steeper than linear, with a slope of 1.23 ± 0.05 (68 % confidence interval).

[21] Calculated using the `emcee` python library (Foreman-Mackey et al. 2013).

[22] The values quoted by García-Burillo et al. (2012) already include systematic uncertainties, so we did not increase the uncertainties on those points.

[23] In this case, we reduced the uncertainties on the García-Burillo et al. (2012) points to remove their estimate for the systematic uncertainties.

In Figure 6 (Right) we perform the same comparison, but utilizing $L'_{HCO^+\ (1-0)}$ instead of $L'_{HCN\ (1-0)}$. As HCO$^+$ (1–0) has a higher critical density than CO (1–0), but lower than HCN (1–0), it is useful to test if it is also linearly tracked by the SFR. The $L'_{HCO^+\ (1-0)}$–L_{IR} relation is also consistent with linear:

$$\log_{10} L_{IR} = (0.94^{+0.25}_{-0.19}) \log_{10} L'_{HCO^+(1-0)} + (3.54^{+2.18}_{-2.20}) \quad (2)$$

Thus, our results are consistent with scenarios in which the HCN and HCO$^+$ emission both trace the dense gas associated with ongoing star formation, albeit with scatter, likely the result of one or more of the excitation mechanisms discussed in Section 4.

5.2. *The Lack of HCO$^+$ Measurements for non-(U)LIRGs*

The inclusion of the Gao & Solomon (2004a) HCN observations adds in a substantial number of galaxies with $L_{IR} < 10^{11}\ L_\odot$, but corresponding HCO$^+$ (1–0) observations are not available. In order to assess the degree to which these lower-luminosity systems influence our fitting results, we also fit the HCN (1–0)–L_{IR} relation without the points from Gao & Solomon (2004a); this fit is shown as the dot-dash line in Fig 7 (Left) and the best-fit relation is:

$$\log_{10} L_{IR} = (1.09^{+0.48}_{-0.31}) \log_{10} L'_{HCN(1-0)} + (2.30^{+3.37}_{-3.64}) \quad (3)$$

which is consistent with that for the full dataset.

5.3. *Dense Gas Depletion Times*

The ratio $L'_{HCN\ (1-0)}/L_{IR}$ is often taken as $\propto M_{dense}/SFR$, which corresponds to the depletion time (τ_{dep}) of the dense molecular gas. In Figure 7 (Left) we show $L'_{HCN\ (1-0)}/L_{IR}$ as a function of L_{IR}, excluding sources which are AGN dominated (PAH EQW $< 0.2\ \mu m$). As in Figure 6 (Left), we include observations from Gao & Solomon (2004a). The mean $log_{10}(L'_{HCN\ (1-0)}/L_{IR}) = 1 \times 10^{-3}$ with a RMS scatter of 0.22 dex. The AGN and starburst dominated systems (as traced by the 6.2 μm PAH feature) have similar $L'_{HCN\ (1-0)}/L_{IR}$ ratios.

Similarly, $L'_{HCO^+\ (1-0)}/L_{IR}$ shows no obvious trend with L_{IR}, but has substantial scatter. The mean $log_{10}(L'_{HCO^+\ (1-0)}/L_{IR}) = 1 \times 10^{-3}$ with a RMS scatter of 0.19 dex.

The significant scatter in $L'_{HCN\ (1-0)}/L'_{HCO^+\ (1-0)}$ can plausibly be attributed to the influence of multiple excitation mechanisms for these dense gas tracers, as described above. These observations are consistent with a scenario in which molecular abundance (Lepp & Dalgarno 1996), density (Meijerink et al. 2007), and radiative effects (Aalto et al. 1995) all influence the global HCN (1–0) emission, obscuring a simple link between $L'_{HCN\ (1-0)}$ and the mass of dense gas directly associated with ongoing star formation. Stated differently, the conversion factor between $L'_{HCN\ (1-0)}$ (or $L'_{HCO^+\ (1-0)}$) and

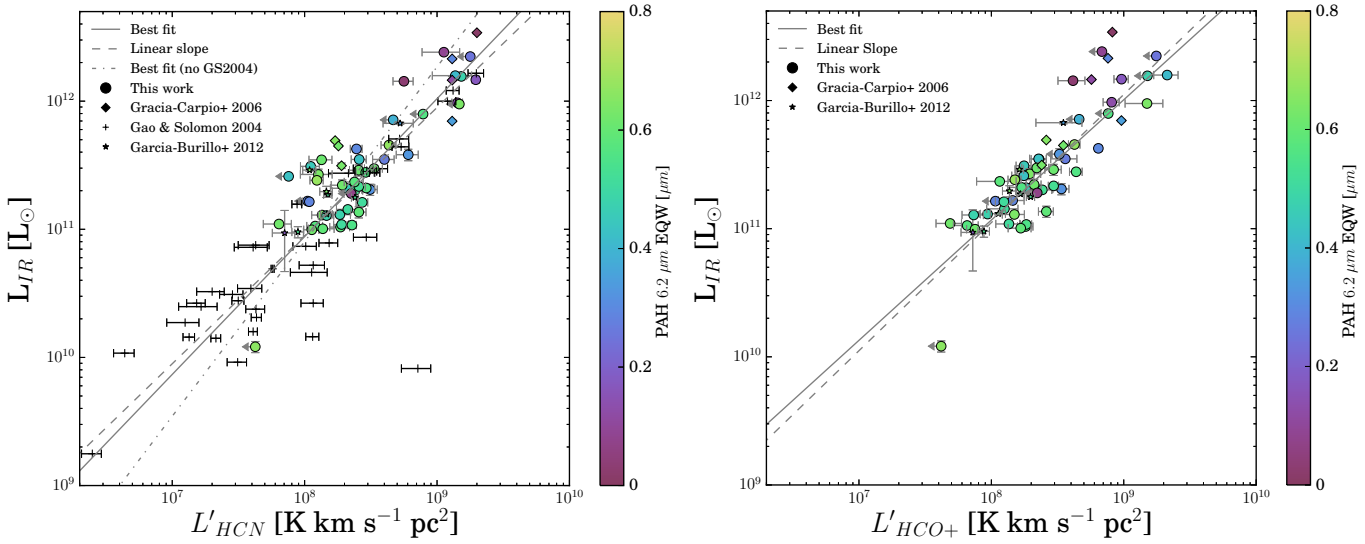

Figure 6. L_{IR} plotted as a function of $L'_{HCN\ (1–0)}$ (Left) and $L'_{HCO^+\ (1–0)}$ (right). The points are color-coded by 6.2 μm EQW. The solid lines in the left and right panels denote the best fit relations of equations 1 and 2, respectively, while the dashed lines show the relation if we fix the slope to be linear. The fits do not include upper limits, but the (solid and dashed) fits to the L_{IR}–$L'_{HCN\ (1–0)}$ relation (left) includes the data from Gao & Solomon (2004b), corrected to our cosmology. In the left panel, we show a fit excluding the Gao & Solomon (2004b) points, as the dot-dash line. We find a slope consistent with being linear, when considering L_{IR} ($L'_{HCN\ (1–0)}$) (Equation 1), consistent with Gao & Solomon (2004b). For L_{IR} ($L'_{HCO^+\ (1–0)}$) we find a slope consistent with a linear relation (Equation 2). The fits do not include upper limits or AGN-dominated systems (PAH EQW $<$ 0.2 μm).

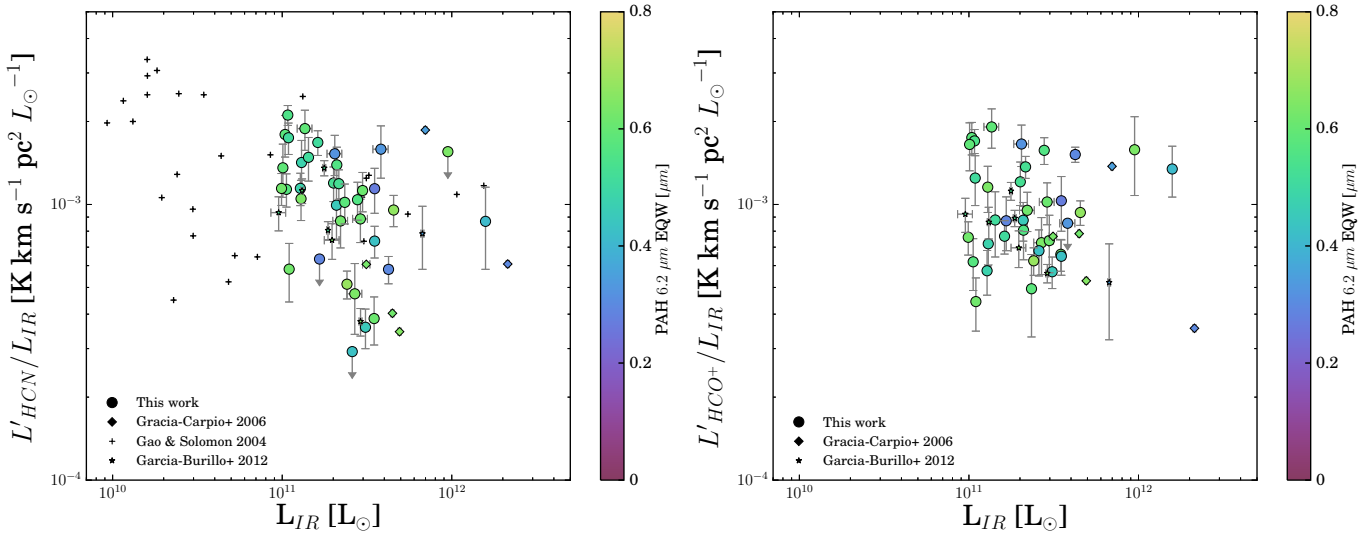

Figure 7. Left: $L'_{HCN\ (1–0)}/L_{IR}$ versus L_{IR}. The Gao & Solomon (2004a) points have been corrected to the cosmology assumed here. Right: $L'_{HCO^+\ (1–0)}/L_{IR}$ versus L_{IR}. Points are color-coded by the 6.2 μm PAH EQW. We see no clear trend of the gas depletion time with L_{IR}.

M_{dense} likely depends on the relative HCN–H_2 abundance in addition to the overall density, excitation source (PDR vs XDR), and influence of infrared pumping. A better understanding of the processes in (U)LIRGs contributing to $L'_{HCN\ (1–0)}$ and $L'_{HCO^+\ (1–0)}$ are needed to determine if the scatter in Figure 7 is due to differences in the consumption rates of molecular gas or a varying $L'_{HCN\ (1–0)}$–M_{dense} conversion factor. Future observations (Section 4.5), coupled with improved modeling, should be able to discriminate between these scenarios for the HCN and HCO^+ emission in (U)LIRGs.

6. SUMMARY

We make use of new measurements of the putative high density gas tracers HCN (1–0) and HCO^+ (1–0) in a sample of local (U)LIRGs. A comparison between the ratios of these lines and the 6.2 μm PAH EQW mid-infrared AGN indicator suggests enhancements in the global HCN (1–0) emission (relative to HCO^+ (1–0)) does not uniquely trace the presence of an energetically dominant AGN. While we find enhanced HCN (1–0)

emission relative to HCO$^+$ (1–0) in objects hosting dominant AGN, we find the same magnitude of enhancement is also possible for systems which are dominated by star formation. The HCN (1–0) and HCO$^+$ (1–0) emission does not seem to be driven by a single process. It is likely that their emission is determined by the interplay of radiation field, gas column, and gas density. This hampers a simple interpretation of the line ratio. Existing data on the X-ray and mid-infrared properties of these systems are not complete or deep enough (respectively) for us to prefer one of XDRs or mid-infrared pumping as the mechanism for enhancing the HCN (1–0) emission.

We compare the HCN (1–0) emission with the star formation rate (L_{IR}) and find a linear relationship, consistent with some previous studies (e.g., Solomon et al. 1992; Gao & Solomon 2004b). However, our result is also consistent with a superlinear relationship, within our 99% confidence interval, analogous to the recent study utilizing L_{FIR}, by García-Burillo et al. (2012). The large scatter in the L'/L_{IR} ratios is consistent with a scenario in which these dense gas tracers can be influenced by density effects, infrared pumping, and/or XDRs. This potentially complicates the determination of global dense gas masses and dense gas depletion times.

We thank the anonymous referee for their careful reading of our manuscript and for their helpful comments and suggestions, which improved the paper.

G.C.P. and A.S.E. were supported by the NSF grant AST 1109475, and by NASA through grants HST-GO10592.01-A and HST-GO11196.01-A from the Space Telescope Science Institute, which is operated by the Association of Universities for Research in Astronomy, Inc., under NASA contract NAS5-26555. G.C.P. and E.T. were supported by the CONICYT Anillo project ACT1101 (EMBIGGEN). G.C.P. was also supported by a Visiting Graduate Research Fellowship at the Infrared Processing and Analysis Center / Caltech and by a FONDECYT Postdoctoral Fellowship (No. 3150361). This work was supported in part by National Science Foundation Grant No. PHYS-1066293 and the hospitality of the Aspen Center for Physics. G.C.P. acknowledges the hospitality of the National Socio-environmental Synthesis Center (SESYNC), where portions of this manuscript were written. A.S.E. was also supported by the Taiwan, R.O.C. Ministry of Science and technology grant MoST 102-2119-M-001-MY3. KI acknowledges support by the Spanish MINECO under grant AYA2013-47447-C3-2-P and MDM-2014-0369 of ICCUB (Unidad de Excelencia "María de Maeztu"). RHI, MAPT, and AA also acknowledge support from the Spanish MINECO through grant AYA2012-38491-C02-02. E.T. was also supported by the Center of Excellence in Astrophysics and Associated Technologies (PFB 06) and by the FONDECYT regular grant 1120061.

This research has made use of the NASA/IPAC Extragalactic Database (NED) which is operated by the Jet Propulsion Laboratory, California Institute of Technology, under contract with the National Aeronautics and Space Administration. This research also made use of Astropy, a community-developed core Python package for Astronomy (The Astropy Collaboration et al. 2013), the `cubehelix` python library[24], and NASA's Astrophysics Data System. The Spitzer Space Telescope is operated by the Jet Propulsion Laboratory, California Institute of Technology, under NASA contract 1407. G.C.P. thanks Ina Evans for a critique of the comments of an earlier version of this manuscript.

Facility: IRAM:30m (EMIR, WIMA, FTS)

REFERENCES

Aalto, S., Booth, R. S., Black, J. H., & Johansson, L. E. B. 1995, A&A, 300, 369
Aalto, S., Booth, R. S., Black, J. H., Koribalski, B., & Wielebinski, R. 1994, A&A, 286, 365
Aalto, S., Spaans, M., Wiedner, M. C., & Hüttemeister, S. 2007, A&A, 464, 193
Aalto, S., et al. 2015, ArXiv e-prints, astro-ph:1504.06824
Armus, L., et al. 2004, ApJS, 154, 178
—. 2007, ApJ, 656, 148
Armus, L., et al. 2009, PASP, 121, 559
Barcos-Muñoz, L., et al. 2015, ApJ, 799, 10
Bigiel, F., Leroy, A., Walter, F., Brinks, E., de Blok, W. J. G., Madore, B., & Thornley, M. D. 2008, AJ, 136, 2846
Brandl, B. R., et al. 2006, ApJ, 653, 1129
Carter, M., et al. 2012, A&A, 538, A89
Costagliola, F., et al. 2011, A&A, 528, A30
Curran, P. A. 2014, ArXiv e-prints, astro-ph:1411.3816
—. 2015
Davies, R. I., Mark, D., & Sternberg, A. 2012, A&A, 537, A133
Diaz-Santos, T., et al. 2013, ApJ, 774, 68
—. 2014, ApJ, 788, L17
Evans, A. S., Solomon, P. M., Tacconi, L. J., Vavilkin, T., & Downes, D. 2006, AJ, 132, 2398
Foreman-Mackey, D., Hogg, D. W., Lang, D., & Goodman, J. 2013, PASP, 125, 306
Gao, Y., & Solomon, P. M. 2004a, ApJS, 152, 63
—. 2004b, ApJ, 606, 271
García-Burillo, S., Usero, A., Alonso-Herrero, A., Graciá-Carpio, J., Pereira-Santaella, M., Colina, L., Planesas, P., & Arribas, S. 2012, A&A, 539, A8
Genzel, R., et al. 1998, ApJ, 498, 579
Ginsburg, A., & Mirocha, J. 2011, Astrophysics Source Code Library, 9001
Graciá-Carpio, J., García-Burillo, S., Planesas, P., & Colina, L. 2006, ApJ, 640, L135
Haan, S., et al. 2011, AJ, 141, 100
Harrison, F. A., et al. 2013, ApJ, 770, 103
Hinshaw, G., et al. 2009, ApJS, 180, 225
Hogg, D. W., Bovy, J., & Lang, D. 2010, ArXiv e-prints, astro-ph:1008.4686
Houck, J. R., et al. 2004, ApJS, 154, 18
Howell, J. H., et al. 2010, ApJ, 715, 572
Huettemeister, S., Henkel, C., Mauersberger, R., Brouillet, N., Wiklind, T., & Millar, T. J. 1995, A&A, 295, 571
Imanishi, M., & Nakanishi, K. 2006, PASJ, 58, 813
—. 2013, AJ, 146, 91
—. 2014, AJ, 148, 9
Imanishi, M., Nakanishi, K., & Kohno, K. 2006, AJ, 131, 2888
Imanishi, M., Nakanishi, K., Tamura, Y., Oi, N., & Kohno, K. 2007, AJ, 134, 2366
Imanishi, M., Nakanishi, K., Tamura, Y., & Peng, C.-H. 2009, AJ, 137, 3581
Inami, H., et al. 2013, ApJ, 777, 156
Iwasawa, K., et al. 2011, A&A, 528, A137
Juneau, S., Narayanan, D. T., Moustakas, J., Shirley, Y. L., Bussmann, R. S., Kennicutt, Jr., R. C., & Vanden Bout, P. A. 2009, ApJ, 707, 1217
Kim, D.-C., et al. 2013, ApJ, 768, 102
Klein, B., Hochgürtel, S., Krämer, I., Bell, A., Meyer, K., & Güsten, R. 2012, A&A, 542, L3
Kohno, K., Ishizuki, S., Matsushita, S., Vila-Vilaró, B., & Kawabe, R. 2003, PASJ, 55, L1

[24] https://github.com/jradavenport/cubehelix

Krips, M., Neri, R., GarcíaBurillo, S., Martín, S., Combes, F., GraciáCarpio, J., & Eckart, A. 2008, ApJ, 677, 262
Lahuis, F., et al. 2007, ApJ, 659, 296
Lepp, S., & Dalgarno, A. 1996, A&A, 306, L21
Leroy, A. K., et al. 2011, ApJ, 739, L25
Leroy, A. K., et al. 2012, AJ, 144, 3
Lu, N., et al. 2014, ApJ, 787, L23
Martín, S., Verdes-Montenegro, L., Aladro, R., Espada, D., Argudo-Fernández, M., Kramer, C., & Scott, T. C. 2014, A&A, 563, L6
Meijerink, R., Spaans, M., & Israel, F. P. 2007, A&A, 461, 793
Mould, J. R., et al. 2000, ApJ, 529, 786
Petric, A. O., et al. 2011, ApJ, 730, 28
Sakamoto, K., Aalto, S., Evans, A. S., Wiedner, M. C., & Wilner, D. J. 2010, ApJ, 725, 8
Sanders, D. B., Mazzarella, J. M., Kim, D.-C., Surace, J. A., & Soifer, B. T. 2003, AJ, 126, 1607
Solomon, P. M., Radford, S. J. E., & Downes, D. 1992, Nature, 356, 318
Stierwalt, S., et al. 2013, ApJ, 206, 1
Teng, S. H., et al. 2014, ApJ, 785, 19
The Astropy Collaboration et al. 2013, A&A, 558, A33

Table 1
IRAM 30m Observing Log

Source	J2000 RA [deg]	J2000 Dec [deg]	z	Obs Month [YYYY-MM]	t_{int} [min]	T$_{sys}$ [K]	Backend
NGC 0034	2.77729	–12.10775	0.0200	2011-09	276	116	WILMA
MCG –02-01-052	4.70904	–10.36246	0.0274	2011-12	127	89	FTS
MCG –02-01-051	4.71208	–10.37672	0.0270	2011-12	277	90	FTS
IC 1623	16.94804	–17.50721	0.0205	2011-12	95	88	FTS
MCG –03-04-014	17.53733	–16.85272	0.0342	2011-12	223	86	FTS
IRAS 01364-1042	24.72050	–10.45317	0.0487	2011-09	117	98	WILMA
IC 214	33.52279	+5.17367	0.0300	2011-12	244	84	FTS
NGC 0958	37.67858	–2.93905	0.0193	2012-10	61	139	FTS
ESO 550-IG 025	65.33333	–18.81094	0.0321	2013-08	298	105	WILMA
UGC 03094	68.89096	+19.17172	0.0247	2012-10	224	126	FTS
NGC 1797	76.93690	–8.01911	0.0149	2012-10	184	113	FTS
VII Zw 031	79.19333	+79.67028	0.0540	2010-06	42	137	WILMA
IRAS F05189-2524	80.25612	–25.36261	0.0435	2011-12	297	107	FTS
IRAS F05187-1017	80.27728	–10.24619	0.0283	2011-12	138	88	FTS
IRAS F06076-2139	92.44088	–21.67325	0.0376	2013-08	127	107	WILMA
NGC 2341	107.30000	+20.60278	0.0174	2014-03	61	89	FTS
NGC 2342	107.32525	+20.63622	0.0174	2012-10	326	107	FTS
IRAS 07251-0248	111.90646	–2.91503	0.0876	2013-08	255	113	WILMA
NGC 2623	129.60045	+25.75461	0.0185	2010-06	42	200	WILMA
IRAS 09111-1007W	138.40167	–10.32500	0.0564	2013-08	318	103	WILMA
IRAS 09111-1007E	138.41167	–10.32231	0.0550	2011-09	117	98	WILMA
UGC 05101	143.96500	+61.35328	0.0394	2010-06	191	116	WILMA
CGCG 011-076	170.30095	–2.98396	0.0247	2012-10	163	123	FTS
IRAS F12224-0624	186.26621	–6.68103	0.0257	2012-10	92	135	FTS
CGCG 043-099	195.46167	+4.33333	0.0374	2011-09	116	98	WILMA
ESO 507-G 070	195.71812	–23.92158	0.0215	2011-12	180	110	FTS
NGC 5104	200.34627	+0.34248	0.0186	2012-10	153	121	FTS
IC 4280	203.22212	–24.20720	0.0165	2012-10	132	145	FTS
NGC 5257	204.97042	+0.84058	0.0227	2014-03	132	104	FTS
NGC 5258	204.98854	+0.82989	0.0226	2011-12	180	88	FTS
UGC 08739	207.30800	+35.25730	0.0172	2012-10	102	111	FTS
NGC 5331	208.06750	+2.10156	0.0330	2013-08	286	98	WILMA
CGCG 247-020	214.93007	+49.23666	0.0258	2014-03	122	153	FTS
IRAS F14348-1447	219.40975	–15.00633	0.0830	2011-09	223	139	WILMA
CGCG 049-057	228.30455	+7.22556	0.0127	2012-10	71	116	FTS
NGC 5936	232.50360	+12.98953	0.0134	2012-10	91	123	FTS
ARP 220	233.73854	+23.50323	0.0181	2010-06	53	159	WILMA
IRAS F16164-0746	244.79913	–7.90078	0.0229	2011-12	201	94	FTS
CGCG 052-037	247.73545	+4.08292	0.0248	2012-10	214	113	FTS
IRAS F16399-0937	250.66754	–9.72067	0.0270	2011-12	191	91	FTS
NGC 6285	254.59998	+58.95594	0.0186	2011-12	127	82	FTS
NGC 6286	254.63146	+58.93673	0.0185	2011-12	53	79	FTS
IRAS F17138-1017	259.14900	–10.34439	0.0175	2011-12	149	102	FTS
UGC 11041	268.71599	+34.77625	0.0161	2012-09	41	101	FTS
CGCG 141-034	269.23598	+24.01704	0.0199	2012-10	61	109	FTS
IRAS 18090+0130	272.91004	+1.52782	0.0293	2013-08	286	94	WILMA
NGC 6701	280.80208	+60.65312	0.0132	2012-10	163	165	FTS
NGC 6786	287.72500	+73.40992	0.0250	2011-09	265	95	WILMA
UGC 11415	287.76833	+73.42556	0.0252	2011-09	287	92	WILMA
ESO 593-IG 008	288.62950	–21.31897	0.0487	2011-09	53	120	WILMA
NGC 6907	306.27750	–24.80893	0.0106	2012-09	102	171	FTS
IRAS 21101+5810	317.87667	+58.38422	0.0398	2013-08	308	89	WILMA
ESO 602-G 025	337.85621	–19.03454	0.0247	2012-10	142	125	FTS
UGC 12150	340.30077	+34.24918	0.0216	2012-10	81	100	FTS
IRAS F22491-1808	342.95567	–17.87357	0.0760	2011-12	158	111	FTS
CGCG 453-062	346.23565	+19.55198	0.0248	2012-10	122	96	FTS
NGC 7591	349.56777	+6.58579	0.0165	2012-10	101	102	FTS
IRAS F23365+3604	354.75542	+36.35250	0.0645	2011-09	32	87	WILMA

Note. — Col 1: Source name, Col 2: Right Ascension, Col 3: Declination, Col 4: redshift, Col 5: Year and month of observation, Col 6: Total on-source time, Col 7: System temperature, Col 8: Backend used for measurements (either the Fourier Transform Spectrometer (FTS; Klein et al. 2012) or the Wideband Line Multiple Autocorrelator (WILMA)).

Table 2
IRAM 30m Fluxes

Source	Σ T$_{mb}dv$ (CCH) [K km s^{-1}]	Σ T$_{mb}dv$ (HCN (1–0)) [K km s^{-1}]	Σ T$_{mb}dv$ (HCO$^+$ (1–0)) [K km s^{-1}]	Σ T$_{mb}dv$ (HNC (1–0)) [K km s^{-1}]
NGC 0034	< 0.35	0.71 ± 0.12	1.14 ± 0.15	< 0.44
MCG –02-01-052	< 0.33	0.57 ± 0.13	< 0.27	< 0.26
MCG –02-01-051	< 0.23	0.17 ± 0.05	0.30 ± 0.07	< 0.16
IC 1623	1.40 ± 0.14	1.51 ± 0.15	4.00 ± 0.15	0.64 ± 0.13
MCG –03-04-014	0.48 ± 0.12	0.94 ± 0.12	0.93 ± 0.09	0.38 ± 0.12
IRAS 01364-1042	< 0.46	< 0.71	< 0.45	< 0.54
IC 214	< 0.15	0.36 ± 0.10	0.56 ± 0.12	< 0.14
NGC 0958	< 0.42	< 0.71	< 0.58	< 0.69
ESO 550-I G025	< 0.35	0.45 ± 0.11	0.36 ± 0.11	< 0.39
UGC 03094	0.63 ± 0.12	< 0.42	0.74 ± 0.14	< 0.41
NGC 1797	< 0.37	0.72 ± 0.17	0.55 ± 0.12	< 0.43
VII Zw 031	< 1.00	< 0.98	1.26 ± 0.40	< 0.96
IRAS F05189-2524	< 0.24	0.73 ± 0.13	0.55 ± 0.13	0.39 ± 0.11
IRAS F05187-1017	0.49 ± 0.12	0.75 ± 0.11	0.76 ± 0.14	< 0.18
IRAS F06076-2139	< 0.60	1.05 ± 0.20	< 0.59	< 0.50
NGC 2341	0.65 ± 0.21	< 0.35	< 0.43	< 0.60
NGC 2342	0.55 ± 0.11	0.68 ± 0.11	0.75 ± 0.13	< 0.22
IRAS 07251-0248	< 0.41	0.35 ± 0.11	< 0.33	< 0.40
NGC 2623	< 1.27	2.62 ± 0.48	2.40 ± 0.54	< 1.23
IRAS 09111-1007W	< 0.36	0.60 ± 0.08	0.83 ± 0.16	< 0.25
IRAS 09111-1007E	0.66 ± 0.16[a]	< 0.36	< 0.41	< 0.35
UGC 05101	0.99 ± 0.20	2.17 ± 0.20	1.25 ± 0.17	0.92 ± 0.20
CGCG 011-076	< 0.51	1.09 ± 0.15	1.20 ± 0.17	< 0.35
IRAS F12224-0624	< 0.69	< 0.55	< 0.67	< 0.66
CGCG 043-099	< 0.55	< 0.54	< 0.53	< 0.53
ESO 507-G 070	< 0.48	1.22 ± 0.19	1.87 ± 0.21	0.49 ± 0.13
NGC 5104	< 0.67	1.23 ± 0.22	0.74 ± 0.20	< 0.41
IC 4280	0.55 ± 0.15	0.95 ± 0.21	1.17 ± 0.23	0.57 ± 0.18
NGC 5257	< 0.29	0.39 ± 0.10	0.46 ± 0.09	0.37 ± 0.11
NGC 5258	< 0.20	0.43 ± 0.10	0.53 ± 0.07	0.30 ± 0.08
UGC 08739	< 0.51	1.30 ± 0.17	0.94 ± 0.19	0.88 ± 0.19
NGC 5331	< 0.31	0.67 ± 0.10	0.45 ± 0.10	< 0.43
CGCG 247-020	< 0.38	0.96 ± 0.15	0.57 ± 0.12	0.35 ± 0.09
IRAS F14348-1447	< 0.46	< 0.52	< 0.37	< 0.51
CGCG 049-057	1.57 ± 0.36	3.21 ± 0.32	1.48 ± 0.20	1.70 ± 0.28
NGC 5936	< 0.48	1.21 ± 0.16	0.81 ± 0.11	< 0.46
ARP 220	4.37 ± 0.62	12.15 ± 0.75	6.02 ± 0.74	7.85 ± 0.60
IRAS F16164-0746	0.65 ± 0.12	0.54 ± 0.11	0.93 ± 0.12	0.32 ± 0.09
CGCG 052-037	0.57 ± 0.12	0.67 ± 0.12	0.74 ± 0.10	0.73 ± 0.13
IRAS F16399-0937	0.66 ± 0.14	0.77 ± 0.10	0.68 ± 0.10	0.38 ± 0.11
NGC 6285	0.38 ± 0.10	< 0.36	< 0.25	< 0.35
NGC 6286	0.93 ± 0.20	1.63 ± 0.22	1.67 ± 0.21	< 0.40
IRAS F17138-1017	1.01 ± 0.17	0.83 ± 0.10	1.03 ± 0.12	0.47 ± 0.11
UGC 11041	< 0.50	1.51 ± 0.26	1.49 ± 0.20	< 0.59
CGCG 141-034	< 0.51	1.01 ± 0.20	< 0.49	< 0.69
IRAS 18090+0130	< 0.30	0.67 ± 0.10	0.78 ± 0.11	0.28 ± 0.08
NGC 6701	< 0.48	2.77 ± 0.22	2.26 ± 0.22	1.16 ± 0.22
NGC 6786	0.30 ± 0.10	0.51 ± 0.08	0.56 ± 0.11	0.35 ± 0.09
UGC 11415	< 0.36	< 0.28	0.54 ± 0.12	< 0.22
ESO 593-IG 008	< 0.77	< 0.98	< 1.22	< 1.05
NGC 6907	< 0.83	2.29 ± 0.31	1.27 ± 0.27	< 0.65
IRAS 21101+5810	0.47 ± 0.11	0.53 ± 0.09	0.33 ± 0.08	< 0.22
ESO 602-G 025	< 0.57	0.84 ± 0.21	0.75 ± 0.12	0.74 ± 0.20
UGC 12150	0.69 ± 0.15	1.36 ± 0.17	1.59 ± 0.14	0.51 ± 0.14
IRAS F22491-1808	< 0.83	< 0.82	< 0.73	< 0.71
CGCG 453-062	0.74 ± 0.14	0.97 ± 0.16	0.48 ± 0.16	< 0.42
NGC 7591	1.37 ± 0.20	1.35 ± 0.18	0.69 ± 0.13	0.68 ± 0.20
IRAS F23365+3604	< 0.58	0.81 ± 0.27	1.28 ± 0.27	< 0.88

Note. — Col 1: Source name, Col 2: CCH (N = 1 $\rightarrow$ 0) flux with 1σ errors, Col 3: HCN (J = 1 $\rightarrow$ 0) flux with 1σ errors, Col 4: HCO$^+$ (J = 1 $\rightarrow$ 0) flux with 1σ errors, Col 5: HNC (J = 1 $\rightarrow$ 0) flux with 1σ errors. The quoted upper limits are 3σ.

[a] Though formally a detection ($> 3\sigma$), this CCH flux appears to be spurious as the signal at the location of CCH is significantly broader than would be expected.

Table 3
Spearman Rank Coefficients

Quantities		ρ	z-score
$L'_{\rm HCN\ (1–0)}/L'_{\rm HCO^+\ (1–0)}$	vs $\log_{10}(L_{\rm IR}/L_\odot)$ (Figure 3)	0.021 ± 0.178	0.057 ± 0.494
$L'_{\rm HCN\ (1–0)}/L'_{\rm HCO^+\ (1–0)}$	vs 6.2 μm PAH EQW (Figure 4, Left)	-0.512 ± 0.127	-1.532 ± 0.464
$L'_{\rm HCN\ (1–0)}/L'_{\rm HCO^+\ (1–0)}$	vs $\log_{10}([\rm C\ II]/L_{\rm FIR})$ (Figure 5)	-0.401 ± 0.142	-1.165 ± 0.458

Note. — Spearman rank coefficients for several relationships discussed in the text along with z-scores. Quantities and their 68% confidence intervals were computed according to the Monte Carlo perturbation plus bootstrapping method (1e5 iterations) discussed by Curran (2014) and using the associated code (Curran 2015). Upper and lower limits for $L'_{\rm HCN\ (1–0)}/L'_{\rm HCO^+\ (1–0)}$ were not included when computing these coefficients.

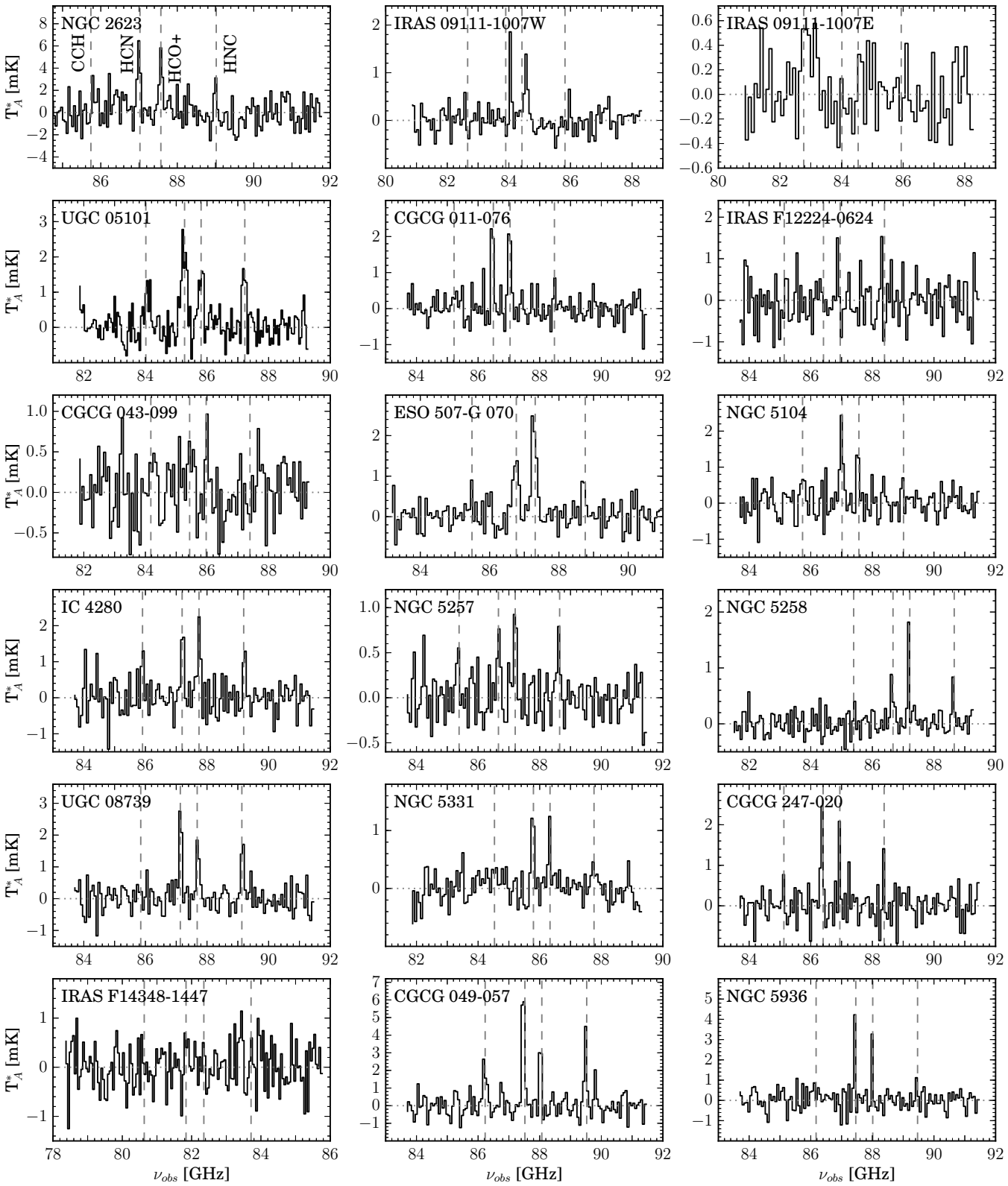

Figure 8. Figure 1 Continued

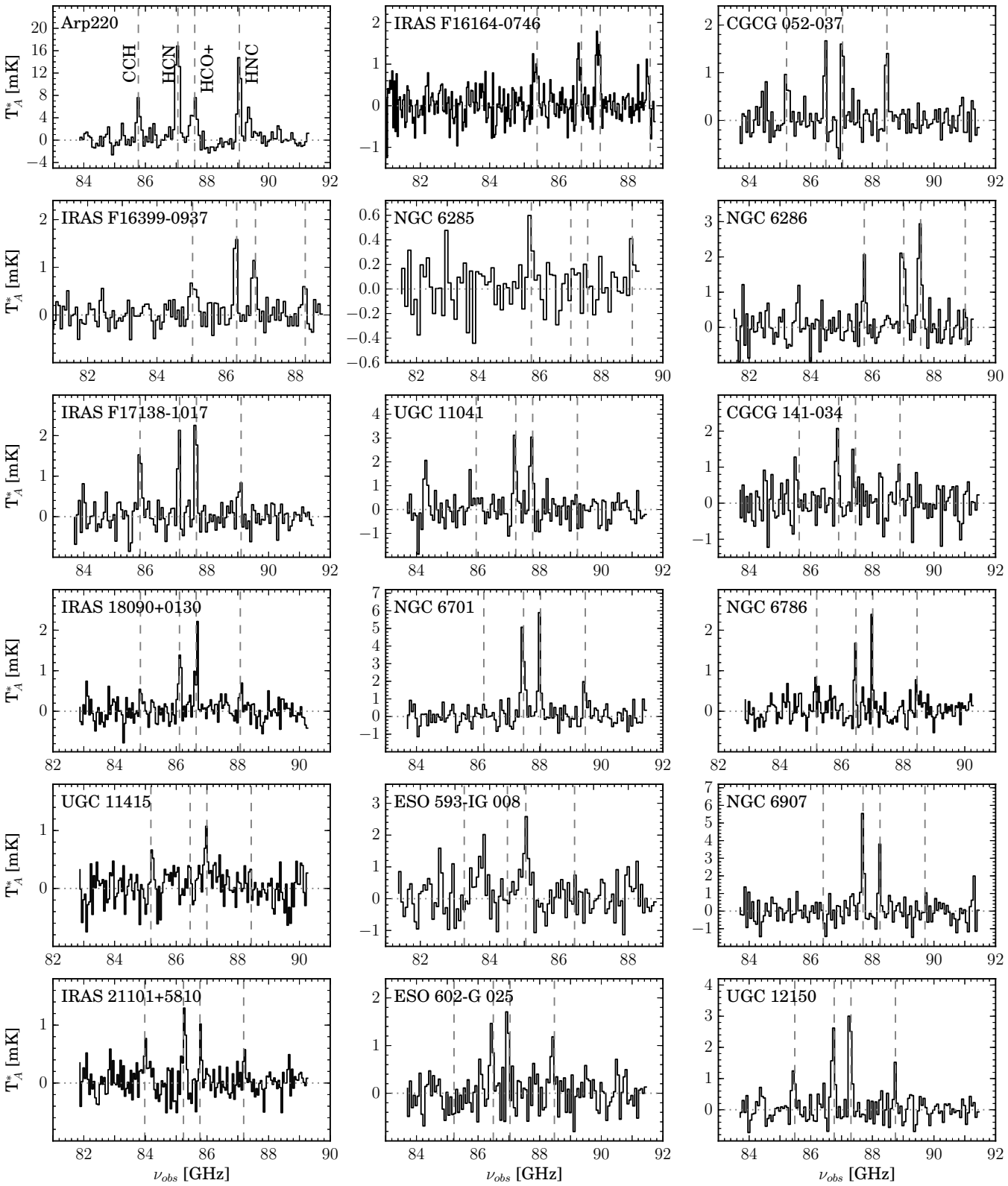

Figure 9. Figure 1 Continued

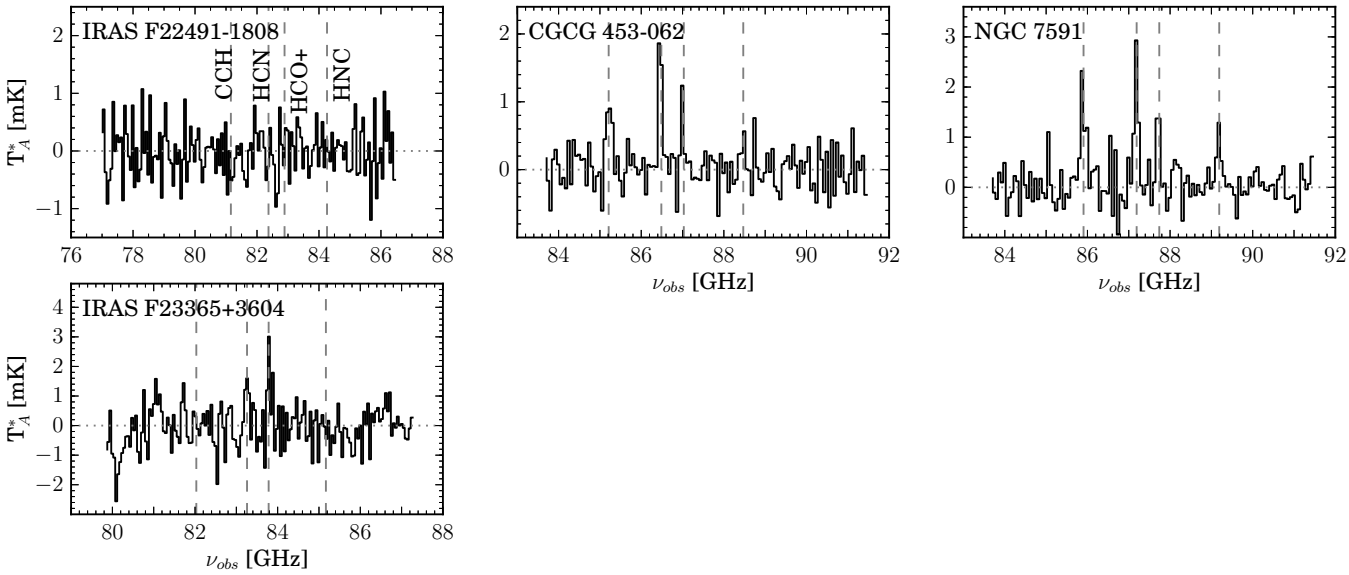

Figure 10. Figure 1 Continued